

Geophysical Research Letters

RESEARCH LETTER

10.1029/2020GL092334

Key Points:

- The oxygen 630-nm emission has been detected in the Mars dayglow with the UVIS-NOMAD/UVIS instrument on board EXOMARS Trace Gas Orbiter
- The 630-nm emission is broadly distributed in the thermosphere with a maximum intensity at the limb of ~4 kiloRayleighs near 150 km
- Photochemical model simulations predict O(1D) and O(1S) densities in agreement with the observed limb profiles

Correspondence to:










J.-C. Gérard,
jc.gerard@uliege.be

Citation:

Gérard, J.-C., Aoki, S., Gkouvelis, L., Soret, L., Willame, Y., Thomas, I. R., et al. (2021). First observation of the oxygen 630 nm emission in the Martian dayglow. *Geophysical Research Letters*, 48, e2020GL092334. <https://doi.org/10.1029/2020GL092334>

Received 29 DEC 2020
 Accepted 19 MAR 2021

First Observation of the Oxygen 630 nm Emission in the Martian Dayglow

J.-C. Gérard¹ , S. Aoki^{1,2} , L. Gkouvelis^{1,3} , L. Soret¹ , Y. Willame², I. R. Thomas² , C. Depiesse², B. Ristic² , A. C. Vandaele², B. Hubert¹, F. Daerden² , M. R. Patel⁴ , J.-J. López-Moreno⁵, G. Bellucci⁶, J. P. Mason⁴, and M. A. López-Valverde⁵ 

¹LPAP, STAR Institute, Université de Liège, Belgium, ²Royal Belgian Institute for Space Aeronomy, Brussels, Belgium, ³NASA/Ames Research Center, Moffett Field, Mountain view, CA, USA, ⁴School of Physical Sciences, The Open University, Milton Keynes, UK, ⁵Instituto de Astrofísica de Andalucía/CSIC, Granada, Spain, ⁶Istituto di Astrofisica e Planetologia Spaziali, INAF, Rome, Italy

Abstract Following the recent detection of the oxygen green line airglow on Mars, we have improved the statistical analysis of the data recorded by the NOMAD/UVIS instrument on board the ExoMars Trace Gas Orbiter mission by summing up hundreds of spectra to increase the signal-to-noise ratio. This led to the observation of the OI 630 nm emission, the first detection in a planetary atmosphere outside the Earth. The average limb profile shows a broad peak intensity of 4.8 kR near 150 km. Comparison with a photochemical model indicates that it is well predicted by current photochemistry, considering the sources of uncertainty. The red/green line intensity ratio decreases dramatically with altitude as a consequence of the efficient quenching of O(¹D) by CO₂. Simultaneous observations of the green and red dayglow will provide information on variations in the thermosphere in response to seasonal changes and the effects of solar events.

Plain Language Summary The green and red oxygen emissions at 557.7 and 630 nm, respectively, are among the dominant spectral features of the terrestrial dayglow and aurora. Recently, the presence of the green emission was also observed in the Martian dayglow using the NOMAD/UVIS instrument on board the ExoMars Trace Gas Orbiter mission. The red line was expected to be significantly weaker as the long-lived upper state of the transition is deactivated by collisions with ambient CO₂. Further statistical treatment of the spectra collected during 1.5 years near solar minimum has led to the discovery of the presence of the 630 nm dayglow emission. The averaged limb profile shows a maximum limb brightness near 150 km about 30 times weaker than the green line. The altitude and brightness of the red emission are in agreement with those simulated with a photochemical model for the same conditions as the observations. The same model also matches the characteristics of the averaged 557.7-nm dayglow profile observed simultaneously. Variations in the characteristics of the oxygen emissions are related to changes in the composition of the Martian upper atmosphere such as those generated by seasons and energetic solar events.

1. Introduction

The first Martian dayglow observations were collected with the ultraviolet spectrometers on board Mariner 6, 7, and 9 flown to Mars in the early 1970s (Barth, 1974). They identified the presence of a series of oxygen and carbon lines and molecular bands originating from CO and CO₂⁺. They obtained limb profiles of the strongest emissions. High quality extreme ultraviolet disk spectra were collected with the Hopkins Ultraviolet Telescope by Feldman et al. (2000). Later, limb observations with the SPICAM instrument on board Mars Express identified N₂ Vegard-Kaplan emissions in the middle ultraviolet (Leblanc et al., 2007). A major step forward was made with the Imaging Ultraviolet Spectrograph (IUVS) spectral imager on board the Mars Atmosphere and Volatile Evolution (MAVEN) spacecraft, which has collected a wealth of ultraviolet limb scans (Jain et al., 2015).

The possible presence of visible dayglow emissions in the Martian dayglow was investigated by Fox and Dalgarno (1979) who modeled the sources and sinks of O(¹S) metastable atoms that produce emission of the green line and trans-auroral emissions at 555.7 and 297.2 nm respectively. They also predicted the

presence of the doublet at 630–636.4 nm produced by radiative relaxation through the $O(^1D) \rightarrow ^3P$ forbidden transition. The $O(^1D)$ state has a long radiative life of about 120 s, which makes it subject to collisional deactivation by CO_2 , O, N_2 , and CO in most of the thermosphere. A consequence is that, although $O(^1D)$ atoms are produced in larger amounts than $O(^1S)$, the intensity of the 630 nm dayglow was expected to be significantly dimmer than the green line. The oxygen red and green lines have been detected in comets since 1966 (Swings, 1962) and in Io's atmosphere (Schneider et al., 1989), but none of them had been observed in planetary atmospheres until Gérard et al. (2020) first reported measurements of the green line airglow with the UltraViolet and Visible Spectrometer (NOMAD/UVIS) on board the Trace Gas Orbiter (TGO) mission of the European Space Agency. Those observations were performed between 24 April and 1 December 2019 when the Mars solar longitude ranged from 16° and 115° . They found that the [OI] 557.7 nm limb profiles present two peaks with the lower and brightest one near 80 km and the upper one in the vicinity of 110 km. They modeled the $O(^1S)$ steady state density distribution and simulated limb observations in close agreement with the UVIS observations. They were not able to identify any spectral features associated with the [OI] 630 nm line at a one-sigma level above the background noise. This absence of red line detection was in agreement with its expected small intensity and the lower instrumental sensitivity at longer wavelengths.

In this study, we present new results related to the search for the presence of the 630 nm emission in spectra obtained by averaging a large fraction of the dayside limb scans made with the UVIS instrument, which is part of the NOMAD suite of instruments (Patel et al., 2017; Vandaele et al., 2018) on board the TGO spacecraft. We determine its peak intensity and provide an estimate of its altitude distribution in the thermosphere. Finally, we compare the observations with those expected from a model simulation adapted to low solar activity periods at aphelion and perihelion.

2. Limb Observations of Oxygen Lines

The methodology adopted for this study is similar to the approach described by Gérard et al. (2020). The TGO spacecraft is on a circular Martian orbit at ~ 400 km inclined by 74° on the planetary equator since October 2016. The UVIS-NOMAD, an ultra-light instrument covering the 200–650 nm spectral range, has both nadir and solar occultation modes. It has been occasionally operated to collect spectra in the “inertial limb” mode where the “nadir channel” points at the dayside limb in a fixed orientation in the inertial space (López-Valverde et al., 2018). By virtue of the spacecraft's latitudinal motion along its orbit, the line of sight scans through the atmosphere from ~ 400 km down to a predetermined altitude of the tangent point, generally close to 20 km. It generates a second limb profile when moving back up again. The integration time of each spectrum is 15 s. The combination of the view angle and the spacecraft motion yields a vertical resolution of 10 ± 5 km near the tangent point.

This procedure has been applied during approximately four orbits per month. A total of 777 spectra at a spectral resolution of ~ 1.5 nm have been gathered between April 2019 and October 2020. Following calibration in physical units and background subtraction using spectra collected at high altitudes, the spectra collected between 100 and 200 km have been co-added to improve the signal-to-noise ratio. The resulting mean spectrum is shown in Figure 1. We observe that the background level increases beyond 300 nm as a consequence of the contribution of scattered solar light. The spectrum shows molecular features such as the CO Cameron bands (180–280 nm), the CO_2^+ UV doublet at 298–299 nm, and several CO_2^+ Fox-Duffen-dack-Barker bands between 300 and 400 nm. The [OI] green line at 557.7 nm stands out with a peak brightness of 173 kR at a tangent height of 82 km (see Table 1).

We now examine the spectrum in the region of the 630 nm line and the insert covering the region 620–640 nm of Figure 1. The background level in the visible part of the spectrum is mostly caused by scattered sunlight from the lower atmosphere. The $1-\sigma$ standard deviation of the background at 620–640 nm (except 630 nm) is equivalent to a radiance of $\sim 2.8 \times 10^{-7}$ $mW m^{-2} sr^{-1} nm^{-1}$ or 1.1 kR nm^{-1} . The counts of an atomic line are distributed over 3 to 4 pixels corresponding to the instrumental point spread function. Radiances exceeding the level of the background standard deviation level are observed in the three adjacent channels extending from 629 to 630.5 nm. The largest of the three values reaches 3.5 times the

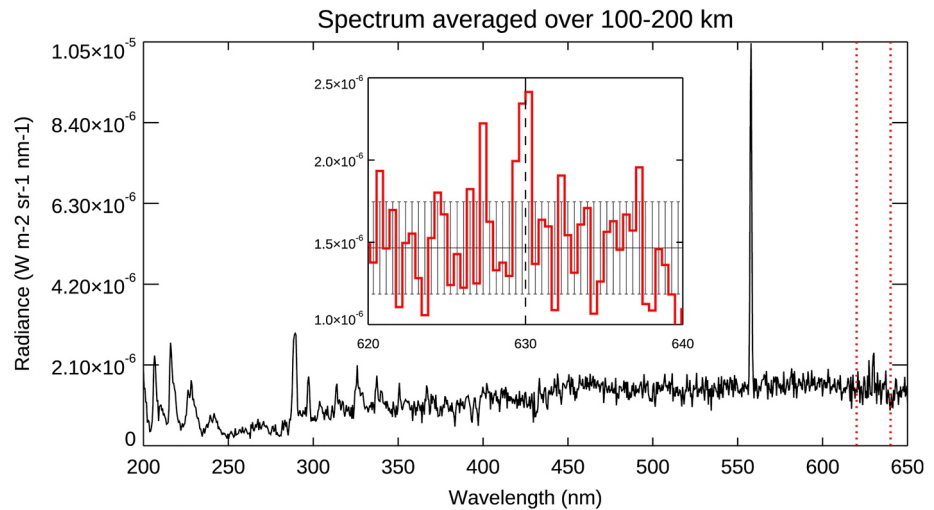


Figure 1. UVIS mean limb spectra averaged between 100 and 200 km of tangent point altitude. The insert is a zoom between 620 and 640 nm showing the detection of the 630 nm forbidden oxygen line (dotted line) reaching 2.3 times the background one-sigma level. UVIS, ultraviolet visible spectrometer.

background 1- σ level. More importantly, the signal extends over 3 spectral channels (as expected from the line spread function) and the sum of the radiances in the 3 channels is equal to 2.3 times the 1- σ level of the background integrated over 3 channels, corresponding to a confidence interval of 98%. We thus conclude that the 630 nm [OI] emission has been detected with a high level of confidence. Further reliance is provided when comparing the limb intensity distribution with model simulations discussed in section 3.

The 630 nm emission is too weak to determine limb profiles based on spectra collected during a single TGO orbit. Instead, we have averaged the observed limb distribution of the global data set and determined the intensity inside 20 km wide altitude bins. The results of the combined spectra are shown in Figure 2 between 100 and 200 km, including a zoom on the 620–640 nm region. We note that the 630 nm feature is observed in all altitude bins, an additional element confirming the reality of its detection. It shows a much broader peak

than other emissions such as CO₂⁺ UVD or the [OI] green line. Table 1 lists the limb intensities averaged in the altitude bins. A 630 nm peak brightness of 4.8 kR is observed in the 120–140 km tangent altitude bin. The 1- σ variability in each altitude bin is indicated in column 4. The large values compared to the mean intensity are a consequence of both the low observed brightness and the true variability due to the combination of observations at different latitudes, solar longitudes, and solar zenith angles. A similar treatment has been applied to the averaged OI 557.7 limb profile with 5-km bins. As described previously by Gérard et al. (2020), the green line limb profile generally shows two peaks. The main one reaches 174 kR and is located at 82 km. The upper peak only appears as an inflexion in the limb brightness at 75 kR near 120 km. The 557.7 nm/630 nm intensity ratio decreases from 33 between 100 and 120 km to about unity at 180–200 km.

The O (¹D → ³P) transition is a doublet with a second component at 636.4 nm that is the factor of 3–3.1 weaker than the one at 630 nm (Froese Fischer & Tachiev, 2004; Sharpee & Slanger, 2006). Based on this ratio, this second line is expected to have a peak limb intensity of ~1.6 kR, a value nearly equal to one standard variation of the background in this spectral region, not observed in Figure 1.

Table 1
Limb Intensity of the [OI] 630 and 557.7 nm Dayglow Emissions

| Line (nm) | Altitude (km) | Intensity (kR) | 1- σ | #Spectra |
|-----------|---------------|----------------|-------------|----------|
| 630 | 80–100 | 3.0 | 2.9 | 290 |
| 630 | 100–120 | 3.2 | 2.6 | 193 |
| 630 | 120–140 | 4.8 | 2.7 | 160 |
| 630 | 140–160 | 4.1 | 2.4 | 145 |
| 630 | 160–180 | 4.4 | 2.0 | 142 |
| 630 | 180–200 | 2.0 | 1.7 | 137 |
| 557.7 | 60–80 | 133 | 17 | 111 |
| 557.7 | 80–100 | 153 | 4.7 | 290 |
| 557.7 | 100–120 | 84 | 3.6 | 193 |
| 557.7 | 120–140 | 57 | 4.6 | 160 |
| 557.7 | 140–160 | 20 | 4.3 | 145 |
| 557.7 | 160–180 | 6 | 3.4 | 142 |
| 557.7 | 180–200 | 3 | 4.4 | 137 |

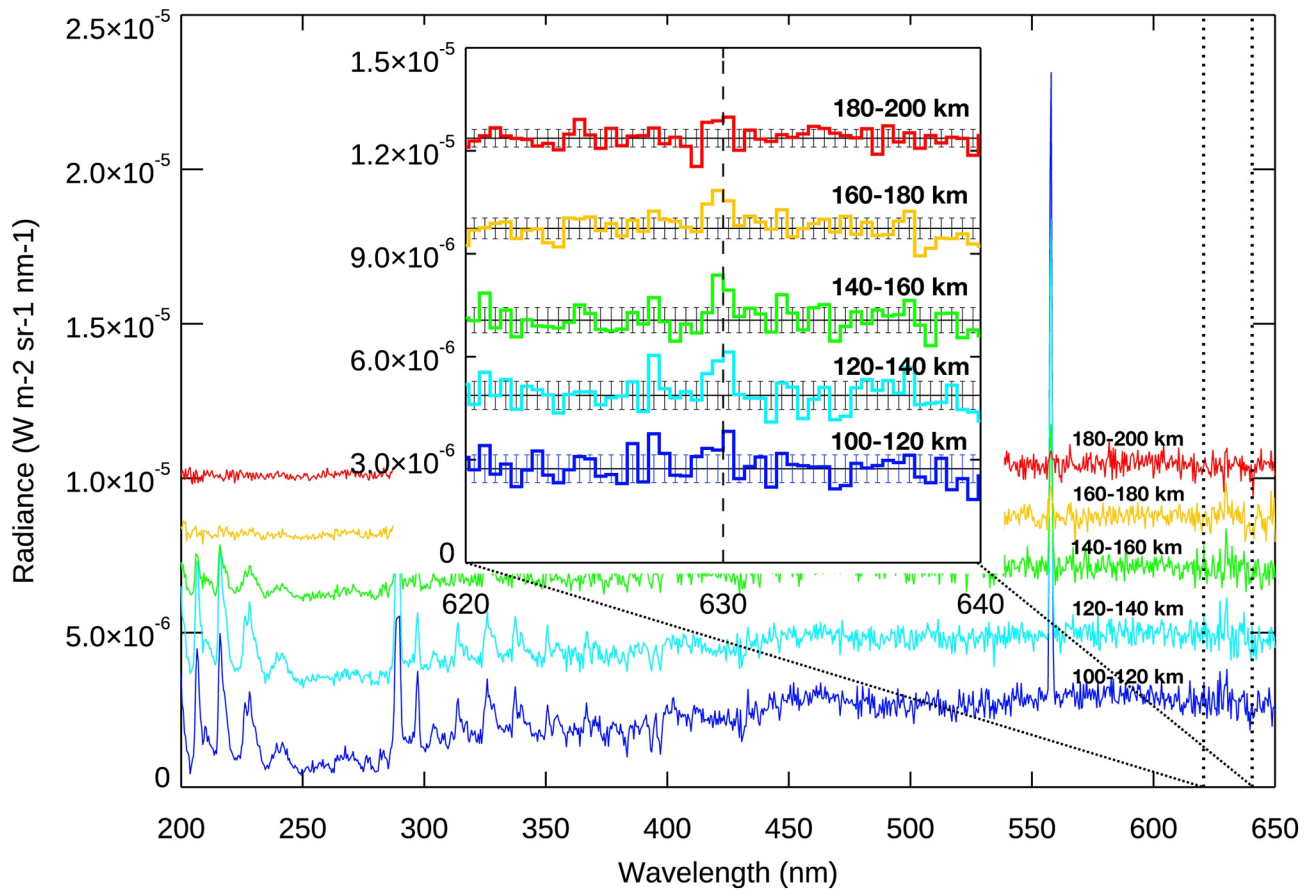


Figure 2. UVIS mean limb spectra averaged in 20-km altitude bins. The insert is a zoom on the 620–640 nm spectral region in the different altitude bins. The dotted line at 630 nm confirms the presence of the oxygen line peak at all five altitudes.

3. Model Simulations for UVIS Observing Conditions

Numerical simulations have been made using the model described by Gkouvelis et al. (2018, 2020a) and Gérard et al. (2019, 2020). The sources of $O(^1D)$ in the Martian upper atmosphere are listed in Table 2. In this Table, e_{th} represents thermal electrons and e_{pe} photoelectrons.

Process (1) is the photodissociation of CO_2 leading to $CO + O(^1D)$ fragments. The wavelength-dependent CO_2 photodissociation rate is calculated as described by Gkouvelis et al. (2018). It is multiplied by the wavelength-dependent quantum yield $\eta(\lambda)$ for the production of $O(^1D)$ fragments. The quantum yield of $O(^1D)$ in the CO_2 photodissociation was investigated by Slinger et al. (1977) and Slinger and Black (1978). We adopt the compilation by Jain (2013).

The extreme ultraviolet solar flux involved in dissociative excitation process (1) and other $O(^1D)$ sources that depend on the EUV flux is calculated using the reconstructed spectra (Thiemann et al., 2017) for the appropriate date, based on EUVM-MAVEN measurements in three ranges made at aphelion, available at <https://pds-ppi.igpp.ucla.edu/search/view/?f=yes&id=pds://PPI/maven.euv.modelled>.

The EUVM instrument provides FISM-M spectrally resolved solar EUV irradiance at Mars from 0.5 to 190 nm every minute at a resolution of 1 nm.

Processes (2), (3), and (4) correspond to photoelectron impact on ground state O, CO_2 , and CO. They are calculated similarly to Gérard et al. (2020), using cross sections taken from Jackman et al. (1977). Laboratory experiments have shown that the quantum yield of $O(^1D)$ by dissociative recombination of O_2^+ (process 5) depends to some extent on the vibrational level of the ion (Fox & Hać, 2009). The value by Kella et al. (1997) for $\nu = 0$ is 1.09 ± 0.15 , while Petrigiani et al. (2005) obtained 0.95 for $\nu = 0$ and $T_e = 500K$, and Peverall

Table 2
Sources and Losses of O(¹D) Atoms in the Martian Upper Atmosphere in the Model

| Number | Process | Rate coefficient |
|-----------------------|--|--|
| Sources | | |
| (1) | CO ₂ + photons → CO + O(¹ D) | σ _{CO₂} (λ), η(λ) (see text) |
| (2) | e _{pe} + O(³ P) → O(¹ D) + e _{pe} | σ ₂ |
| (3) | e _{pe} + CO ₂ → CO + O(¹ D) + e _{pe} | σ ₃ |
| (4) | e _{pe} + CO → C + O(¹ D) + e _{pe} | σ ₄ |
| (5) | O ₂ ⁺ + e _{th} → O([*]) + O(¹ D) | α ₅ = 2.4 × 10 ⁻⁷ (300/Te) ^{0.7} cm ³ s ⁻¹ |
| (6) | CO ₂ ⁺ + e _{th} → CO + O(¹ D) | α ₆ = 2.5 × 10 ⁻⁷ (300/Te) ^{0.46} cm ³ s ⁻¹ |
| (7) | O(¹ S) → O(¹ D) + hν _{557.7 nm} | A _{557.7 nm} = 1.34σ ⁻¹ |
| (8) | O(¹ S) + e _{th} → O(¹ D) + e _{th} | k ₈ = 8.6 × 10 ⁻⁹ cm ³ s ⁻¹ |
| Loss processes | | |
| (9) | O(¹ D) → O(³ P) + hν _{630 nm} | A _{630 nm} = 6.5 × 10 ⁻³ σ ⁻¹ |
| (10) | O(¹ D) → O(³ P) + hν _{636.4 nm} | A _{636.4 nm} = 2.2 × 10 ⁻³ σ ⁻¹ |
| (11) | O(¹ D) + CO ₂ → O(³ P) + CO ₂ | k ₁₁ = 7.5 × 10 ⁻¹¹ exp(115/T) cm ³ s ⁻¹ |
| (12) | O(¹ D) + O ₂ → O(³ P) + CO | k ₁₂ = 3.3 × 10 ⁻¹¹ exp(55/T) cm ³ s ⁻¹ |
| (13) | O(¹ D) + N ₂ → O(³ P) + N ₂ | k ₁₃ = 2.15 × 10 ⁻¹¹ exp(110/T) cm ³ s ⁻¹ |
| (14) | O(¹ D) + CO → O(³ P) + O ₂ | k ₁₄ = 1 × 10 ⁻¹¹ cm ³ s ⁻¹ |
| (15) | O(¹ D) + O(³ P) → 2 O(³ P) | k ₁₅ = 2.13 × 10 ⁻¹² + 2.6 × 10 ⁻¹³ T ^{0.5} - 2.24 × 10 ⁻¹⁵ T cm ³ s ⁻¹ |

et al. (2001) measured 1.17 ± 0.05 . We adopt a value equal to unity, coupled with a total recombination coefficient $\alpha_5 = 2.4 \times 10^{-7} (300/Te)^{0.7} \text{ cm}^3 \text{ s}^{-1}$ (Peverall et al., 2001). This value closely agrees with the ab initio recombination coefficient into the O(¹D) state of $2.2 \times 10^{-7} (300/Te)^{0.46}$ calculated by Guberman (1988). For process (6), the recombination coefficient of CO₂⁺ from Viggiano et al. (2005) equal to $4.2 \times 10^{-7} (300/Te)^{0.75}$ is combined with the O(¹D) quantum yield of 0.6 adopted from S. K. Jain (2013). Process (6) is a secondary source due to the relatively low abundance of CO₂⁺ ions compared to O₂⁺. Source (7), radiative cascade from the ¹S to the ¹D level, is equal to the volume emission rates at 557.7 nm. The coefficient k₈ for the quenching of O(¹S) leading to O(¹D) is taken from Berrington and Burke (1981).

Loss processes (9) and (10) are emissions of 630 and 636.4 nm photons. The rate coefficients for collisional deactivation with CO₂, O₂, and N₂ (11–14) are taken from NASA-JPL recommendation–evaluation 19 by Burkholder et al. (2020). The rate coefficient k₁₄ for quenching by CO is adopted from Schofield (1978) and k₁₅ from Yee et al. (1990).

The neutral density and temperature distributions are adopted from the Mars Climate Database based on the Laboratoire de Météorologie Dynamique three-dimensional model (Forget et al., 1999; González-Galindo et al., 2005). They correspond to the low latitude and low solar activity conditions of the UVIS observations at aphelion (25 August 2019, Ls = 71°) and perihelion (3 August 2020, Ls = 251°). Figure 3 (a) shows the altitude distribution of the main constituents at the equator for the solar minimum condition at aphelion and a solar zenith angle of 30°. The O(¹D) sources are represented in panel (b). The main production below ~130 km is photodissociation of CO₂, followed by radiative cascade from O(¹S) and O₂⁺ dissociative recombination. Panel (c) presents the O(¹D) loss frequency, dominated by processes (9), (10), and (11), with negligible contributions from quenching with other species than CO₂. At photochemical equilibrium, the O(¹D) number density n(O ¹D) is given by the total production rate divided by the loss frequency, and the volume emission rate is equal to the A_{630 nm} n(O ¹D) product. The vertical distribution of the O(¹D) emission rate is presented in panel (d). It shows a broad peak near 170 km resulting from the combination of a production peak at 80 km and a large quenching rate by CO₂ at low altitude.

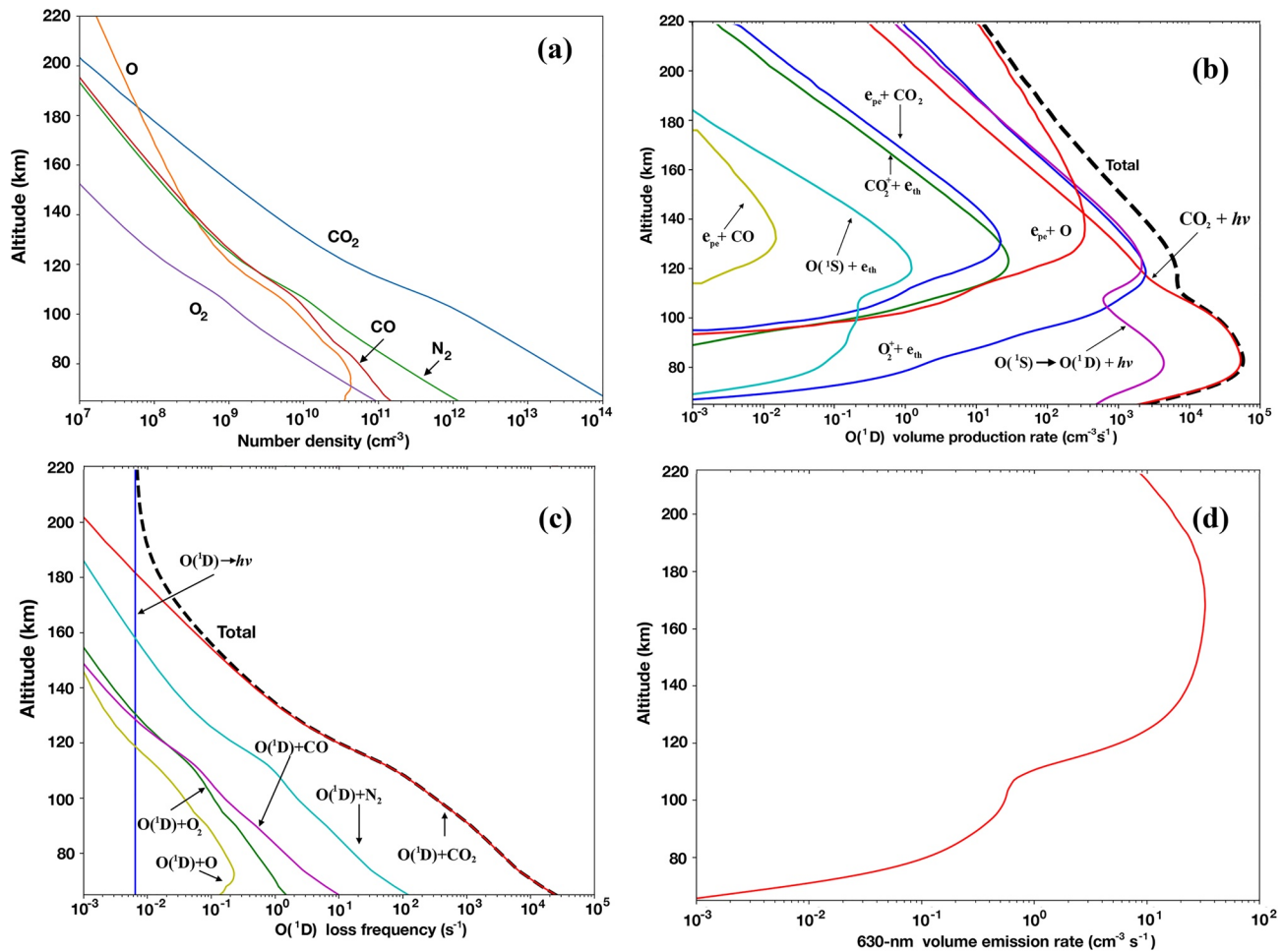


Figure 3. Altitude distribution of the number densities of neutral species (a), $\text{O}(^1\text{D})$ main sources (b), $\text{O}(^1\text{D})$ sinks (c), and 630 nm volume emission rate (d) in the Martian dayglow calculated for solar minimum conditions at aphelion, for a solar zenith angle of 30° .

4. Comparison with UVIS Dayglow Model

The 630 nm emission rate integrated along the line of sight is shown in Figure 4 for aphelion and perihelion and solar zenith angles of 30° and 70° respectively. These conditions encompass those prevailing during the period of observations of the limb profiles averaged here. All curves monotonically increase with altitude up to ~ 150 km where they reach peak values between 4.5 and 5.8 kR. Only the intensities corresponding to $\text{SZA} = 30^\circ$ at perihelion are somewhat higher than the other three cases. For comparison, the mean intensities in 20-km bins of the UVIS 630 nm emission are represented by the red dots, together with their associated $1-\sigma$ uncertainty. The model intensities are in good agreement with the UVIS measurements, considering the uncertainties on the UVIS calibration and the cross sections and the rate coefficients, usually unclaimed, used in the model.

For comparison, the 557.7 nm simulated limb profiles for a range of conditions met during the observations are also shown in Figure 4 for aphelion and perihelion, together with the UVIS averaged limb profile, also based on the same 777 spectra as used in Figure 1. The mean value in 5-km wide bins is shown with the one-sigma uncertainty on the mean. The modeled green line limb profile has been smoothed to account for the finite value of the UVIS view angle. In this case, the peak intensity and the modeled value are in close agreement with a calculated altitude in the model ranging from 65 to 85 km, dependent on the distance to the sun and solar zenith angle.

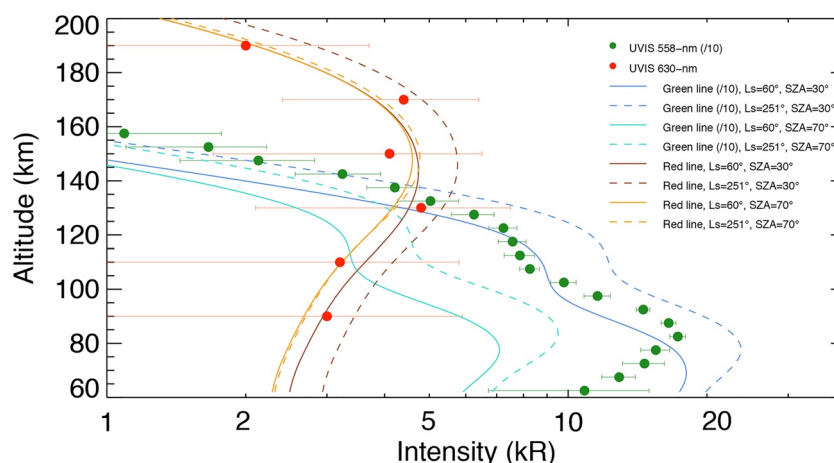


Figure 4. Model calculation of the [OI] 630 nm dayglow limb intensity for two different solar zenith angles (orange and brown curves) at aphelion (solid lines) and perihelion (dashed lines). The 20-km binned brightness of the UVIS observations is shown by the red dots. The green dots are the observed 557.7 nm intensities and the green and blue lines show the modeled profiles for different solar zenith angles and distance from the sun.

5. Conclusions

We report the first measurement of the $[OI] \ ^1D \rightarrow \ ^3P$ transition at 630 nm in the dayglow of another planet performed with the NOMAD/UVIS spectrograph on board TGO. This result is based on 777 co-added spectra binned into 20-km altitude intervals. This emission is considerably weaker than the 557.7 nm line, but the combination of a large number of spectra collected over 18 months makes it possible to specify some of the dayglow characteristics. The emission shows a broad peak around 150 km reaching about 4 kR. The same group of combined spectra exhibits a 557.7-nm peak emission of ~ 150 kR. The large difference between the distribution of the two oxygen lines is not caused by a lower $O(^1D)$ production rate but results from the much longer radiative lifetime of $O(^1D)$ atoms relative to 1S . The weakness of the 630 nm emission does not allow the determination of its latitudinal-seasonal variation at this point. Variability is expected in response to solar activity, distance from the sun, and changes in the atmospheric structure and composition.

Comparison with photochemical modeling indicates that the production and loss of metastable $O(^1D)$ and $O(^1S)$ atoms in the Martian thermosphere appear well understood. Therefore, future observations from UVIS and future space missions will be able to remotely monitor the simultaneous variability of the three oxygen lines (297.2, 557.7, and 630 nm) in complement to molecular bands probing lower altitudes. In particular, it is expected that large-scale perturbations of the thermosphere during solar energetic events, aurora, or possibly global dust storms (Gkouvelis et al., 2020b) may modify the vertical distribution of the dayglow visible emissions. High-resolution measurements of the red line profile are also a potential tool to monitor the temperature of the Martian thermosphere.

Data Availability Statement

The NOMAD-UVIS spectra may be downloaded from ESA's PSA archives at <https://archives.esac.esa.int/psa/#!Table%20View/NOMAD=instrument> (select UVIS from the list of instruments and "Level 3 Calibrated" from the processing level). Only UVIS occultations and dayside nadirs are available at the time of writing; other observation types will be available soon. The EUV-MAVEN solar radiance values are available at <https://pds-ppi.igpp.ucla.edu/search/view/?f=yes&id=pds://PPI/maven.euv.modelled>. Observed limb intensities and model calculations supporting Figure 4 are available from BIRA-IASB repository <https://dx.doi.org/10.18758/71021063> or from the corresponding author upon reasonable request.

References

Barth, C. A. (1974). The atmosphere of Mars. *Annual Review of Earth and Planetary Sciences*, 2(1), 333–367. <https://doi.org/10.1146/annurev.ea.02.050174.002001>

Acknowledgments

B.H. is a research associate and S.A. is a postdoctoral researcher of the Belgian Fund for Scientific Research (FNRS). ExoMars is a space mission of the ESA and Roscosmos. The NOMAD experiment is led by the IASB-BIRA, assisted by Co-PI teams from Spain (IAA-CSIC), Italy (INAF-IAPS), and the United Kingdom (The Open University). This project acknowledges funding from BELSPO, with the financial and contractual coordination by the ESA PRODEX Office (PEA grant numbers 4000103401 and 4000121493). M.A.L.-V. and J.-J.L.-M. were supported by grant number PGC2018-101836-B-100 (MCIU/AEI/FEDER, EU) and by the Spanish Science Ministry Centro de Excelencia Severo Ochoa Program under grant number SEV-2017-0709. M.R.P. and J.P.M. were funded by the UK Space Agency under grants ST/V002295/1, ST/V005332/1, ST/S00145X/1, and ST/R005761/1. G.B. thanks the Italian Space Agency through grant number 2018-2-HH.0. We are grateful to ESA's TGO team and its project scientist H. Svedhem for his support. The authors thank both reviewers for their valuable comments.

- Berrington, K. A., & Burke, P. G. (1981). Effective collision strengths for forbidden transitions in e-N and e-O scattering. *Planetary and Space Science*, 29, 377–381. [https://doi.org/10.1016/0032-0633\(81\)90026-x](https://doi.org/10.1016/0032-0633(81)90026-x)
- Burkholder, J. B., Sander, S. P., Abbatt, J. P. D., Barker, J. R., Cappa, C., Crouse, J. D., & Orkin, V. L. (2020). *Chemical kinetics and photochemical data for use in atmospheric studies; evaluation number 19*. Jet Propulsion Laboratory, National Aeronautics and Space Administration.
- Feldman, P. D., Burgh, E. B., Durrance, S. T., & Davidsen, A. F. (2000). Far-ultraviolet spectroscopy of venus and mars at 4 Å resolution with the Hopkins Ultraviolet Telescope on Astro-2. *Acta Pathologica Japonica*, 538, 395–400. <https://doi.org/10.1086/309125>
- Forget, F., Hourdin, F., Fournier, R., Hourdin, C., Talagrand, O., Collins, M., et al. (1999). Improved general circulation models of the Martian atmosphere from the surface to above 80 km. *Journal of Geophysical Research*, 104(E10), 24155–24175. <https://doi.org/10.1029/1999je001025>
- Fox, J. L., & Dalgarno, A. (1979). Ionization, luminosity, and heating of the upper atmosphere of Mars. *Journal of Geophysical Research*, 84(A12), 7315–7333. <https://doi.org/10.1029/ja084ia12p07315>
- Fox, J. L., & Hać, A. B. (2009). Photochemical escape of oxygen from Mars: A comparison of the exobase approximation to a Monte Carlo method. *Icarus*, 204, 527–544. <https://doi.org/10.1016/j.icarus.2009.07.005>
- Froese Fischer, C., & Tachiev, G. (2004). Breit-Pauli energy levels, lifetimes, and transition probabilities for the beryllium-like to neon-like sequences. *Atomic Data and Nuclear Data Tables*, 87, 1–184. <https://doi.org/10.1016/j.adt.2004.02.001>
- Gérard, J. C., Aoki, S., Willame, Y., Gkouvelis, L., Depiesse, C., Thomas, I. R., & Mason, J. (2020). Detection of green line emission in the dayside atmosphere of Mars from NOMAD-TGO observations. *Nature Astronomy*, 124, 5–8. <https://doi.org/10.1029/2019JA026596>
- Gérard, J. C., Gkouvelis, L., Ritter, B., Hubert, B., Jain, S. K., & Schneider, N. M. (2019). MAVEN-IUVS observations of the CO₂⁺ UV doublet and CO Cameron bands in the Martian thermosphere: Aeronomy, seasonal, and latitudinal distribution. *Journal of Geophysical Research: Space Physics*, 124, 5816–5827. <https://doi.org/10.1029/2019ja026596>
- Gkouvelis, L., Gérard, J. C., González-Galindo, F., Hubert, B., & Schneider, N. M. (2020b). Isobar Altitude Variations in the Upper Mesosphere Observed With IUVS-MAVEN in Response to Martian Dust Storms. *Geophysical Research Letters*, 47(12). e2020GL087468. <https://doi.org/10.1029/2020gl087468>
- Gkouvelis, L., Gérard, J.-C., Ritter, B., Hubert, B., Schneider, N. M., & Jain, S. K. (2018). The O(¹S) 297.2-nm dayglow emission: A tracer of CO₂ density variations in the Martian lower thermosphere. *Journal of Geophysical Research: Planets*, 123(12), 3119–3132. <https://doi.org/10.1029/2018JE005709>
- Gkouvelis, L., Gérard, J. C., Ritter, B., Hubert, B., Schneider, N. M., & Jain, S. K. (2020a). Airglow remote sensing of the seasonal variation of the Martian upper atmosphere: MAVEN limb observations and model comparison. *Icarus*, 341, 113666. <https://doi.org/10.1016/j.icarus.2020.113666>
- González-Galindo, F., López-Valverde, M. A., Angelat i Coll, M., & Forget, F. (2005). Extension of a Martian general circulation model to thermospheric altitudes: UV heating and photochemical models. *Journal of Geophysical Research*, 110. E09008. <https://doi.org/10.1029/2004JE002312>
- Guberman, S. L. (1988). The production of O(¹D) from dissociative recombination of O₂⁺. *Planetary and Space Science*, 36, 47–53. [https://doi.org/10.1016/0032-0633\(88\)90145-6](https://doi.org/10.1016/0032-0633(88)90145-6)
- Jackman, C. H., Garvey, R. H., & Green, A. E. S. (1977). Electron impact on atmospheric gases, I. Updated cross sections. *Journal of Geophysical Research*, 82(32), 5081–5090. <https://doi.org/10.1029/JA082i032p05081>
- Jain, S. K. (2013). *Dayglow emissions on Mars and Venus*, Ph.D. Thesis. Ph.D. Thesis. Cochin University of Science and Technology. <https://dyuthi.cusat.ac.in/jspui/handle/purl/3688>
- Jain, S. K., Stewart, A. I. F., Schneider, N. M., Deighan, J., Stiepen, A., Evans, J. S., et al. (2015). The structure and variability of Mars upper atmosphere as seen in MAVEN/IUVS dayglow observations. *Geophysical Research Letters*, 42, 9023–9030. <https://doi.org/10.1002/2015GL065419>
- Kella, D., Vejby-Christensen, L., Johnson, P. J., Pedersen, H. B., & Andersen, L. H. (1997). The source of green light emission determined from a heavy-ion storage ring experiment. *Science*, 276, 1530–1533. <https://doi.org/10.1126/science.276.5318.1530>
- Leblanc, F., Chaufray, J. Y., Bertaux, J. L., Witasse, O., & Bertaux, J.-L. (2007). On Martian nitrogen dayglow emission observed by SPICAM UV spectrograph/Mars Express. *Geophysical Research Letters*, 34. E09S11. <https://doi.org/10.1029/2006GL028437>
- López-Valverde, M. A., Gérard, J. C., González-Galindo, F., Vandaele, A. C., Thomas, I., Korabiev, O., & Guilbon, S. (2018). Investigations of the Mars upper atmosphere with ExoMars trace gas orbiter. *Space Science Reviews*, 214(1), 29. <https://doi.org/10.1007/s11214-017-0463-4>
- Patel, M. R., Antoine, P., Mason, J., Leese, M., Hathi, B., Stevens, A. H., et al. (2017). NOMAD spectrometer on the ExoMars trace gas orbiter mission: part 2-design, manufacturing, and testing of the ultraviolet and visible channel. *Applied Optics*, 56(10), 2771–2782. <https://doi.org/10.1364/ao.56.002771>
- Petrigiani, A., Hellberg, F., Thomas, R. D., Larsson, M., Cosby, P. C., & van der Zande, W. J. (2005). Electron energy-dependent product state distributions in the dissociative recombination of O₂⁺. *The Journal of Chemical Physics*, 122. 234311. <https://doi.org/10.1063/1.1937388>
- Peeverall, R., Rosén, S., Peterson, J. R., Larsson, M., Al-Khalili, A., Vikor, L., et al. (2001). Dissociative recombination and excitation of O₂⁺: Cross sections, product yields and implications for studies of ionospheric airglows. *The Journal of Chemical Physics*, 114(15), 6679–6689. <https://doi.org/10.1063/1.1349079>
- Schneider, N. M., Shemansky, D. E., & Yu, K. C. (1989). Search for [O I] 6300-Å emission from Io. *Bulletin of the American Astronomical Society*, 21, 988–989. [https://doi.org/10.1016/0016-3287\(89\)90008-6](https://doi.org/10.1016/0016-3287(89)90008-6)
- Schofield, K. (1978). Rate constants for the gaseous interaction of O(²D₂) and O(²S₀) - A critical evaluation. *Journal of Photochemistry*, 9, 55–68. [https://doi.org/10.1016/0047-2670\(78\)87006-3](https://doi.org/10.1016/0047-2670(78)87006-3)
- Sharpee, B. D., & Slanger, T. G. (2006). O(¹D₂₋₃P_{2,1,0}) 630.0, 636.4, and 639.2 nm Forbidden emission line intensity ratios measured in the terrestrial nightglow. *Journal of Physics, Chemistry A*, 110(21), 6707–6710. <https://doi.org/10.1021/jp056163x>
- Slanger, T. G., & Black, G. (1978). CO₂ photolysis revisited. *The Journal of Chemical Physics*, 68(4), 1844–1849. <https://doi.org/10.1063/1.435905>
- Slanger, T. G., Sharpless, R. L., & Black, G. (1977). CO₂ photodissociation, 1060–1175 Å. *The Journal of Chemical Physics*, 67(11), 5317–5323. <https://doi.org/10.1063/1.434710>
- Swings, P. (1962). Comportement des raies interdites de l'oxygène dans les comètes. I: Observations. *Annales d'Astrophysique*, 25, 165–170.
- Thiemann, E. M. B., Chamberlin, P. C., Eparvier, F. G., Templeman, B., Woods, T. N., Bougher, S. W., & Jakosky, B. M. (2017). The MAVEN EUVM model of solar spectral irradiance variability at Mars: Algorithms and results. *Journal of Geophysical Research: Space Physics*, 122, 2748–2767. <https://doi.org/10.1002/2016JA023512>
- Vandaele, A. C., Neefs, E., Drummond, R., Thomas, I. R., Daerden, F., López-Moreno, J. J., & Altieri, F. (2018). Science objectives and performances of NOMAD, a spectrometer suite for the ExoMars TGO mission. *Planetary and Space Science*, 119, 233–249.

- Viggiano, A. A., Ehlerding, A., Hellberg, F., Thomas, R. D., Zhaunerchyk, V., Geppert, W. D., et al. (2005). Rate constants and branching ratios for the dissociative recombination of CO_2^+ . *The Journal of Chemical Physics*, *122*, 226101. <https://doi.org/10.1063/1.1926283>
- Yee, J. H., Guberman, S. L., & Dalgarno, A. (1990). Collisional quenching of $\text{O}(^1\text{D})$ by $\text{O}(^3\text{P})$. *Planetary and Space Science*, *38*(5), 647–652. [https://doi.org/10.1016/0032-0633\(90\)90071-w](https://doi.org/10.1016/0032-0633(90)90071-w)